Tailoring rigidity of bending-active perforated sheets

Eszter FEHÉR[*a,b], Zsófia GYETVAI[a]

[a] Department of Morphology and Geometric Modeling, Budapest University of Technology and Economics

[*,b] HUN-REN-BME Morphodynamics Research Group, Budapest University of Technology and Economics
1111 Budapest Muegyetem rkp. 1-3.
feher.eszter@epk.bme.hu

Abstract

Kirigami is a paper technique that inspires the design of three-dimensional shapes from flat sheets perforated by carefully placed cuts. This study explores the mechanical properties of bending-active kirigami structures formed as a result of perforated sheets buckling into 3D elastica shapes. While design strategies to control the shape of the resulting structure received much attraction, a comprehensive exploration of their mechanical attributes remains lacking. Our investigation focuses on perforated sheets clamped at two ends and subjected to concentrated loads along their symmetry axis. Rigidity analysis reveals two competing effects that influence the structure's behavior. Perforation weakens the structure by reducing local bending stiffness through material removal. However, decreased local bending stiffness can facilitate higher local curvatures, leading to a more favorable shape in terms of rigidity. We explored these effects by employing both numerical simulations and physical experiments on laser-cut PET sheets. Our findings indicate that solely assessing the amount of removed material is insufficient for accurately comparing the rigidity of two patterns. Depending on the cut pattern, a structure with more perforations may exhibit higher rigidity than a less perforated one.

Keywords: perforated kirigami, kirigami surface, geometric rigidity, rigidity control

1. Introduction

The Japanese paper technique known as kirigami enables the creation of three-dimensional structures from flat sheets through strategic cuts, inspiring engineers to develop flat sheets that can transform into various geometries. Applying in-plane compression to a flat sheet induces deformation into the elastica shape, which holds numerous engineering applications ranging from temporary architectural installations [1, 2] to robotic grippers [11]. Shape control can be achieved by altering the initial geometry of the flat sheet or by modifying the local bending stiffness. Liu et al. introduced a framework for the inverse design of the tapered elastica [5], and subsequent work extended this approach to perforated sheets, resulting in arches and domes [4]. Similarly, Ye et al. utilized incisions on rectangular sheets to achieve prescribed shapes of arches and domes [3]. These techniques have been demonstrated to yield typical architectural shapes [5, 4].

Apart from shape design, the analysis and control of the mechanical properties of kirigami structures are equally crucial. The effect of the internal structure on bending stiffness was examined by Marmo et al. [6] for tessellated shells, while Cho et al. [10] examined spatially varying hinges on kirigami surfaces. Shrimali et al. [13] analyzed the bending properties of perforated sheets, whereas Celli et al. [7] and Mcmahan et al. [8] examined architected sheets influenced by the kirigami technique. With nearly infinite possible configurations based on the cut pattern and transformation method used to create

kirigami structures, investigations into the rigidity of various kirigami structures have been conducted, including pop-up kirigami shapes [9, 12], with only a few experiments focusing on perforated elastica shapes.

Zhang et al. [4] performed a rigidity analysis of perforated patterns deforming into domes with various aspect ratios, highlighting the non-monotonic nature of their geometric rigidity. This study delves deeper into this phenomenon by investigating a simpler problem: the bending-active, elastica-shaped arch formed by the compression of long, rectangular, porous flat sheets. We anticipate observing an intricate geometric rigidity behavior resulting from the interplay between local weakening and improved, more favorable geometry controlled by the location of the holes. Employing a one-dimensional nonlinear beam model, we introduce a method to incorporate the holes' effects in the structure. Various patterns were designed and analyzed both numerically and experimentally. First, we evenly distributed holes on the surface to explore the impact of material removal. Subsequently, while keeping the total hole volume constant, we altered only the location of the holes. Finally, applying the insights gained, we designed patterns to demonstrate that the quantity and positioning of the holes comparably impact the structural rigidity.

2. Theoretical background

We consider a rectangular, perforated, initially flat sheet of length L, width w, and thickness t (Figure 1a). The ends of the sheet are clamped, and they are subjected to both horizontal and vertical forces. The distance between the supports is $b < L$. The resulting structure is a bending-active arch and takes the so-called elastica shape (Figure 1b). The shape is described by the angle of its tangent $\theta(s)$ along its arc length $s \in [0, L]$. Here, we consider sheets with constant width and thickness featuring rectangular perforations. The holes are positioned so that both longitudinal and transverse symmetry of the sheet are maintained. Depending on the location of the holes, certain parts of the sheet may become inactive. The load-bearing portion of the sheet, referred to as the effective part, is characterized by the effective width $w_{\text{eff}}(s)$.
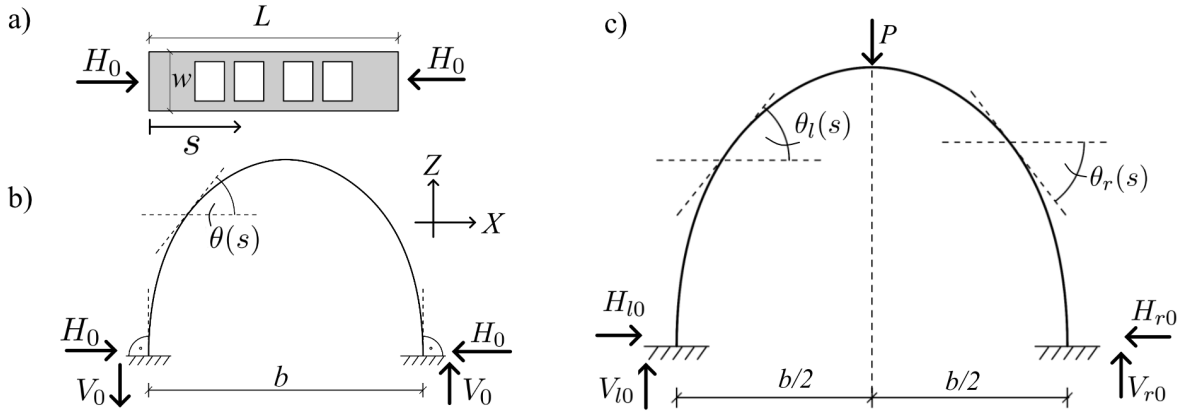

Figure 1: a) Perforated rectangular sheet subjected to horizontal load. b) The sheet deforms into the elastica shape by prescribing $\Delta L = L - b$ displacement. c) The resulting elastica shape under a concentrated load applied at the midpoint of the structure.

The problem can be modeled using the nonlinear beam theory [14] or 'tapered elastica' equation [5]. In

the absence of other external forces acting on the structures, the equilibrium equation is given by:

$$-E\frac{\mathrm{d}}{\mathrm{d}s}\left[I_{\text{eff}}(s)\cdot\frac{\mathrm{d}\theta(s)}{\mathrm{d}s}\right] = V_0\cos\theta(s) + H_0\sin\theta(s), \tag{1}$$

where E is the Young's modulus, $I_{\text{eff}}(s) = w_{\text{eff}}(s)t^3/12$ is the moment of inertia, and V_0, H_0 are the vertical and horizontal support reaction forces, respectively. Rather than specifying the forces applied at the supports, we prescribe the distance between the clamps. Furthermore, we also prescribe that the angle at the supports is vertical. If a concentrated force P is applied at the midpoint of the structure, we can partition the structure into two segments and apply (1) separately for each segment (Figure 1c). Let $\theta_l(s_l)$ represent the angle of the left segment, where $s_l \in [0, L/2]$, and $\theta_r(s_r)$ denote the angle of the right segment, where $s_r \in [L/2, L]$. There are five boundary conditions:

$$\theta_l(0) = \pi/2 = -\theta_r(L), \tag{2}$$

$$L - \Delta L = \int_0^{L/2} cos(\theta_l) + \int_{L/2}^L cos(\theta_r) = b, \tag{3}$$

$$\int_0^{L/2} \sin(\theta_l) + \int_{L/2}^L \sin(\theta_r) = 0, \tag{4}$$

$$\theta_l(L/2) = \theta_r(L/2), \tag{5}$$

$$\frac{\mathrm{d}}{\mathrm{d}s}\theta_l = \frac{\mathrm{d}}{\mathrm{d}s}\theta_r, \tag{6}$$

where (5) and (6) ensure that the tangent and the bending moment are continuous at the midpoint. We further ensure the balance of vertical and horizontal forces by prescribing

$$V_{l0} = V_{r0} + P, \tag{7}$$

$$H_{l0} = H_{r0}. \tag{8}$$

where V_{l0} and V_{r0}, H_{l0}, and H_{r0} represent the vertical and horizontal support reaction forces at the left and right ends, respectively.
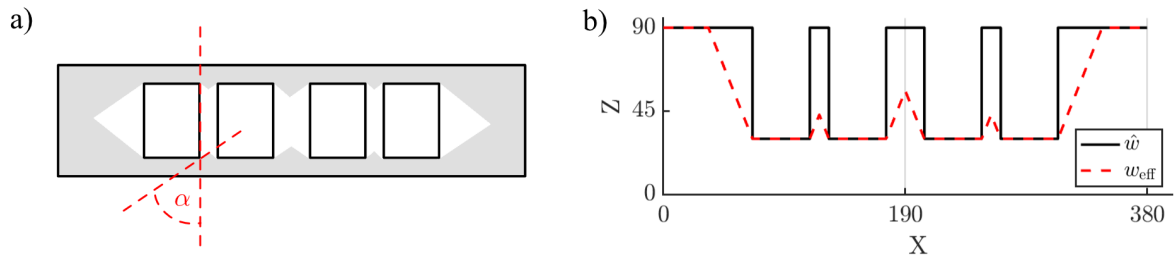

Figure 2: a) Schematic view of the effective area. The grey area represents the effective part of the sheet. The red dashed lines indicate the effective angle α. b) Width of the solid part of the same pattern (black line), and effective width (red dashed line).

It is reasonable to assume that the effective width is not simply the total $\hat{w}(s)$ width of the solid part of the sheet, as certain parts of the sheet do not participate in balancing the forces. To address this, we introduce the concept of the effective angle $0 \leq \alpha \leq \pi/2$, which represents the angle of the line delineating the active and inactive regions (refer to Figure 2a). In the case of $\alpha = 0$, $w_{\text{eff}} = \hat{w}$, i.e., all points of the solid part contribute to balancing the forces, while for $\alpha = \pi/2$, the effective width equals

the minimum width of the solid part $w_{\text{eff}} = \min(\hat{w})$. The effective width is the width of the effective part, i.e., the remaining width after cutting off the solid part at an α angle around the holes (Figure 2b). Following Zhang et. al [4], we adopt the term 'global porosity' as the volume fraction of the holes $\Phi = (A_0 - \hat{A})/A_0$, where $A_0 = Lw$ is the area of the bounding rectangle, and $\hat{A}$ denotes the area of the solid part of the sheet. Similarly, the local porosity is $\varphi(s) = (w - w_{\text{eff}}(s))/w$.

We employed the pde2path [15] and chebfun [16] toolboxes in Matlab to solve the equations. The equations are solved using spectral discretization via Chebyshev polynomials and numerical continuation. The solution process involves two steps: initially, continuation in b, followed by continuation in P to achieve the desired state.

3. Experiments

3.1. Setup

The experimental configuration is depicted in Figure 3. Various patterns were fabricated by laser-cutting from Polyethylene terephthalate (PET) sheets with a thickness of $t = 0.5\,\text{mm}$. The Young's modulus, approximated as $E = 2800\,\text{N/mm}^2$, was obtained from literature data [17], while the density $\rho = 1.33\,\text{g/cm}^3$ was provided by the manufacturer. Each specimen had a total length of $L_{\text{tot}} = 380\,\text{mm}$ and a width of $w = 90,\text{mm}$. Clamping was achieved by utilizing $e = 10\,\text{mm}$ lengths at both ends of the sheets, resulting in an actual arc length of $L = 360\,\text{mm}$ (see Figure 3a). The supports consisted of two vertical metal sheets covered with foamed plastic and secured together using screws, facilitating precise support positioning. A circular hole with a diameter of $5\,\text{mm}$ was situated at the center of the sheets to accommodate a concentrated force applied via a small screw hanger. The fixture's self-weight was $G_s = 6\,\text{g}$ and was present even in the unloaded state for technical reasons.
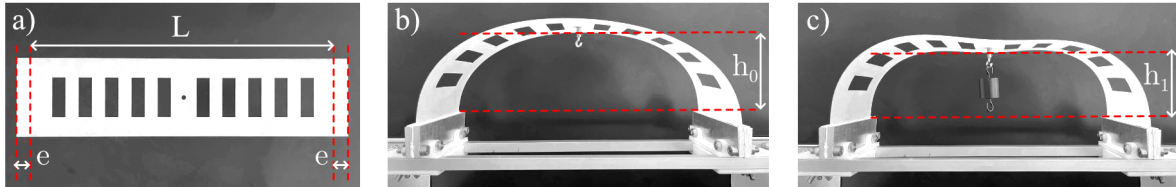

Figure 3: Experimental setup to measure the rigidity of bending-active arches made of perforated sheets. a) The laser-cut PET sheet with $e = 10\,\text{mm}$ extensions on either end. b) Unloaded case and maximal height h_0. c) Loaded case and maximal loaded height h_1. A screw hanger holds a mass at the middle point of the sheet.

We optically measured the maximal height h_0, h_1 of the unloaded and loaded structures, respectively (Figure 3b,c). Subsequently, the structural rigidity was estimated by $K = F/d$, where $d = h_0 - h_1$ represents the deformation, and F denotes the applied load. The self-weight of the sheet is not negligible if the length of the sheet is longer than the elasto-gravitational length [18]

$$l_g = \left(\frac{B}{\rho g t}\right)^{1/3} = \left(\frac{Et^2/12}{\rho g t}\right)^{1/3} = 170.42\,\text{mm} < L, \tag{9}$$

meaning that it is necessary to incorporate the effect of the self-weight in the calculations. We approximated the self-weight by a concentrated load. Accordingly, it is included in P as

$$P_0 = \rho t \hat{A} + G_s, \tag{10}$$

$$P_1 = P_0 + F, \tag{11}$$

utilized in (7) for the unloaded and loaded scenarios, respectively.

3.2. Model validation

3.2.1. Solid sheet

Initially, we examined the solid case ($\Phi = 0$) under gradually increasing loads for distances $b_1 = 3/4L$ and $b_2 = L/2$ (refer to Figure 4). Despite minor asymmetry observed in the experimental results, the deformed shapes closely match the computed ones. Both $F - d$ diagrams are approximately linear in the beginning, validating the use of a linear formula for K for sufficiently small F values.
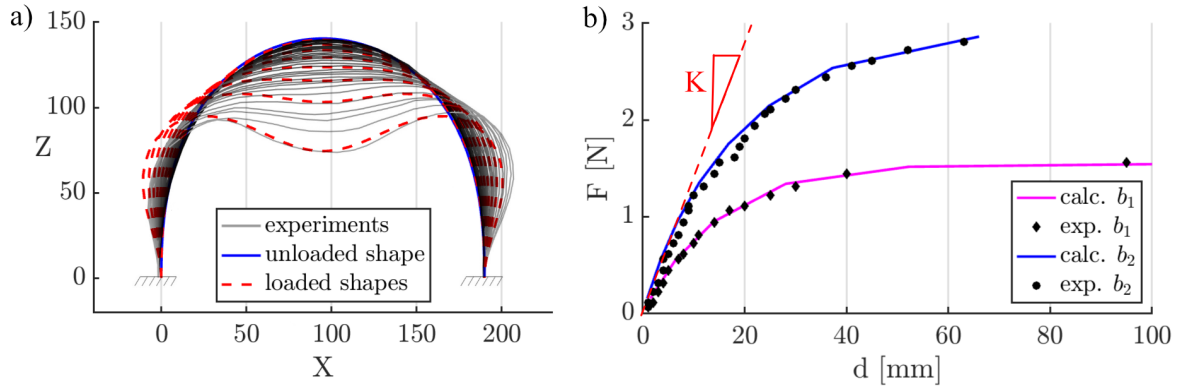

Figure 4: Comparison of experimental and numerical results of solid sheets ($\Phi = 0$). a) Deformation of a sheet with b_2 distance between the supports. The gray lines represent the sheet's shape under discrete, increasing load values observed optically. The blue line depicts the unloaded shape in the calculations, while the red dashed lines illustrate the loaded shapes under increasing load values. b) Comparison of the experimentally measured and numerically calculated force-displacement diagrams for two different support distances b_1 and b_2. For sufficiently small loads, the diagram is approximately linear.

3.2.2. Effective width

Three different symmetric patterns were designed, each possessing the same $\Phi, \hat{w}$ values to examine how the transverse position of a hole affects the rigidity (Figure 5).
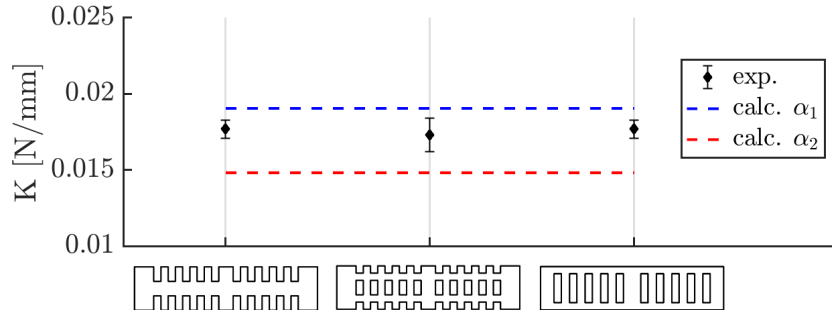

Figure 5: Rigidity assessment of arches with $b = 3/4L$ under a load of $F = 0.38\,\text{N}$. All patterns have identical Φ and $\hat{w}$ values but differ in transverse hole positions. The black diamonds represent experimental results along with their standard deviation. In the calculations, all patterns utilize the same w_{eff} functions. Two different effective angles, $\alpha_1 = \pi/4$ and $\alpha_2 = 2\pi/3$, were considered.

The method illustrated in Figure 2 does not differentiate between these three patterns; all have the same effective width. Experimental findings indicate that the transverse placement of the holes has a minimal impact on the arch's rigidity. Mechanical considerations suggest that $\pi/4 \leq \alpha \leq 2\pi/3$. Accordingly, calculations were conducted using two α values. The difference between the patterns is negligible.

4. Results and discussion

In the following, we present the experimental and numerical results for different patterns while keeping $b = 3/4L$ and $F = 0.38\,\text{N}$ constant. The calculations were conducted using $\alpha_1 = \pi/4$ and $\alpha_2 = 2\pi/3$ values.

4.1. Effect of global porosity

Generally, rigidity and global porosity are inversely proportional. Zhang et al. [4] demonstrated that increasing global porosity leads to a reduction in the rigidity of bending-active porous domes. We examined the effect of global porosity on two different series of patterns (Figure 6). The holes are evenly distributed along the longitudinal direction in both series. In the first series, the number of holes and their length remain constant, but their width gradually increases until they merge (Figure 6a). In the second series of patterns, all holes are $1\,\text{mm} \times 60\,\text{mm}$ rectangles, and their quantity increases (see Figure 6b). In agreement with the literature, the rigidity is inversely proportional to the global porosity in these cases. The calculations and experiments show good agreement.
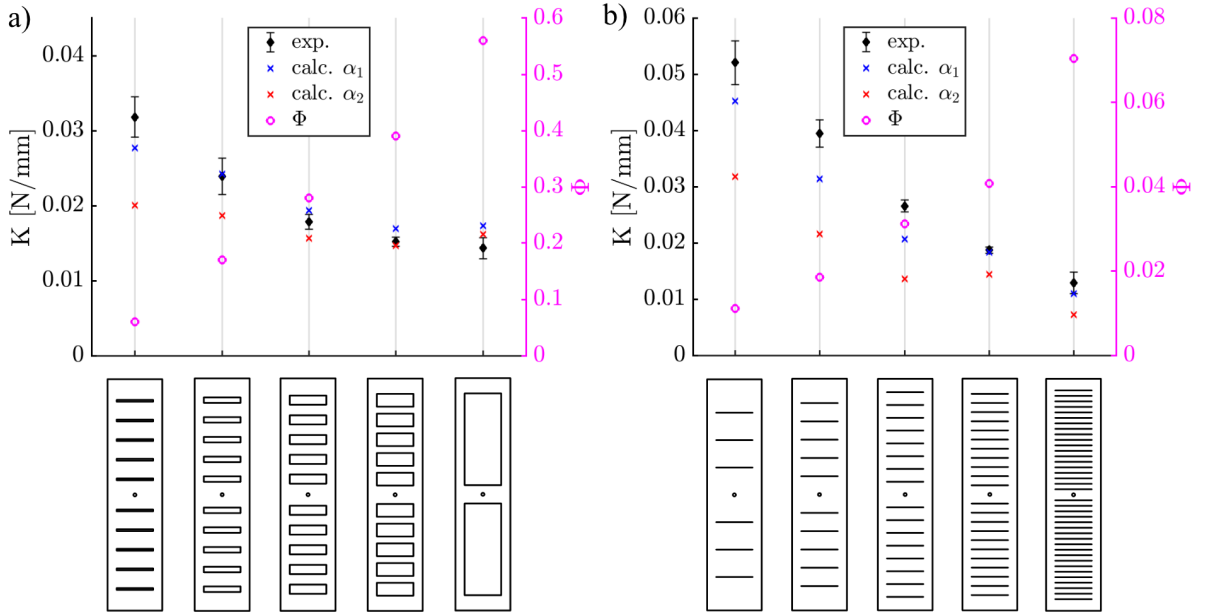

Figure 6: Experimental and numerical analysis of the effect of global porosity on the rigidity. Rigidity values obtained from experiments are represented by black diamonds and shown along with their standard deviation. Numerical results were obtained using two different effective angles. The rigidity and the global porosity are inversely proportional in both series of patterns in the experiments and the calculations. a) In the first series, the number of holes remains constant, but their width gradually increases until they merge. b) In the second series, the size of the holes remains fixed while their number increases.

4.2. Effect of local porosity

To explore the impact of local porosity, we maintained Φ constant by altering the position and dimensions of the holes while preserving their total area (see Figure 7). In the first series of patterns, the size of the holes changes in the longitudinal direction along the sheet, resulting in increased local porosity either around the supports or the concentrated load (Figure 7a). A minimal difference was observed in the rigidity among the various patterns, indicating a preference for hole placement towards the center rather than near the supports. Additionally, Figure 7b demonstrates nearly identical unloaded shapes observed in the experiments.

In the subsequent series of patterns, variations in hole sizes were introduced along the transverse direction (see Figure 7c). Here, a more pronounced distinction was observed between the different patterns. Allowing for a reduced effective width around the center resulted in a narrower unloaded shape with increased height, while cutting wider holes near the supports yielded a lower and broader unloaded shape (see Figure 7d). As a result, the local porosity affects the shape of the structure. Placing holes in advantageous positions can result in a favorable unloaded shape with increased rigidity. This phenomenon can be explained by the increase in curvature at sections with narrower widths. Removing material from the center of the structure enhances its height and, consequently, improves rigidity.
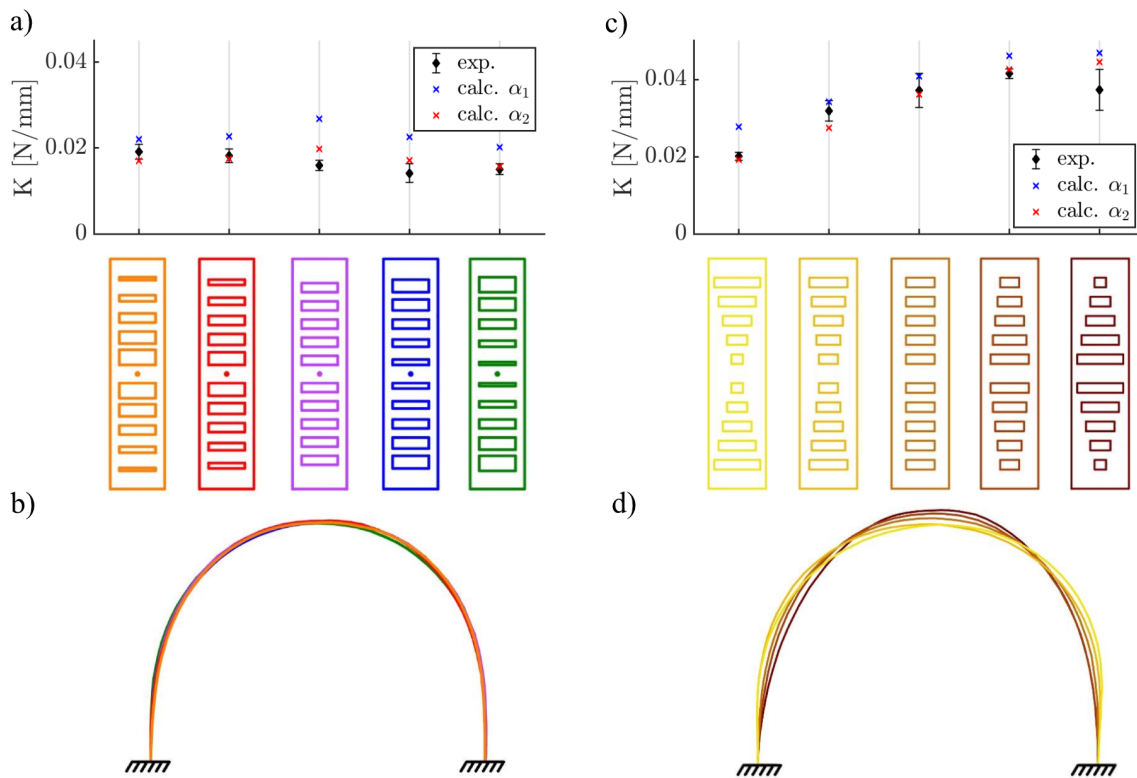

Figure 7: Experimental and numerical analysis of the effect of local porosity on the rigidity ($\Phi = \mathrm{const}$). a) The first series of patterns: the size of the holes is fixed transversally and changes in the other direction. b) Experimentally observed unloaded shapes for the first set of patterns plotted on each other. Color coding follows the colors of the patterns in the image above. c) The second set of patterns: The size of the holes is fixed longitudinally and changes in the other direction. d) Experimentally observed unloaded shapes for the second set of patterns plotted on each other. Color coding follows the colors of the patterns in the image above.

4.3. Rigidity control

Upon comparing the findings from Sections 4.1. and 4.2., it is apparent that both local and global porosity influence the rigidity in the same order of magnitude. Therefore, merely comparing the global porosity is insufficient for predicting which pattern results in greater rigidity. In the third series of experiments, we tailored patterns to validate this statement. By concurrently adjusting both the local and global porosity of the patterns, we discovered that strategically positioning holes can increase the porosity in a way that the rigidity also increases.
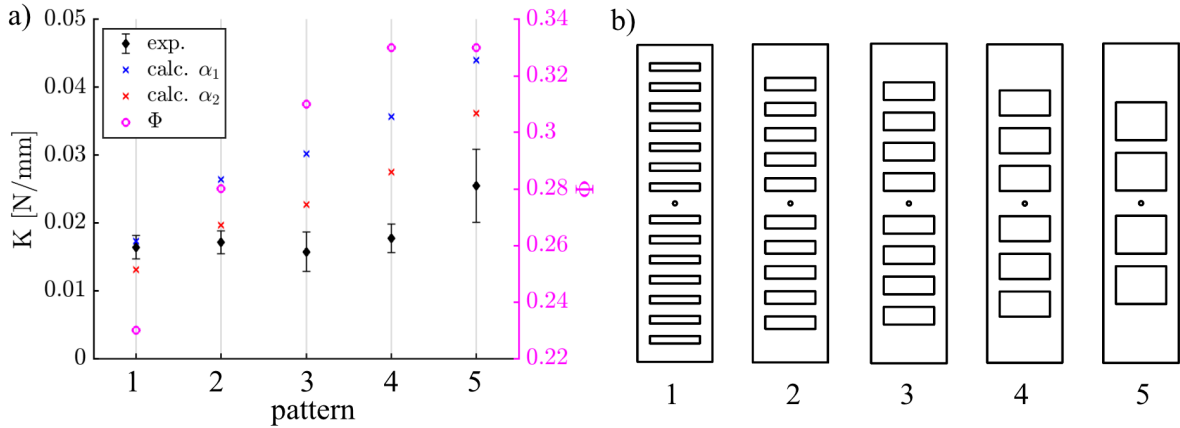

Figure 8: a) Experimental and numerical analysis of patterns with simultaneously changing global and local porosity. b) Numbering of the patterns.
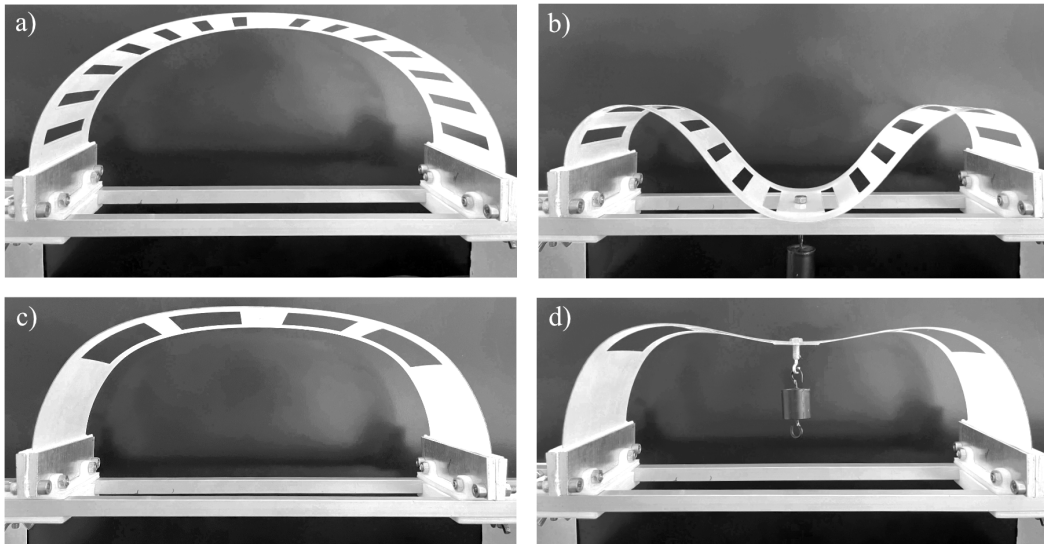

Figure 9: Experimental investigation of Patterns 1 and 5 for $b = 3L/4$ and $F = 0.5N$. a)-b) Unloaded and loaded the shape of Pattern 1. The structure failed under the applied load, and the middle point sank below the line of the supports. c)-d) Unloaded and loaded the shape of Pattern 2 under the same load.

We designed five patterns characterized by simultaneously increasing porosity and rigidity (Figure 8). The longitudinal arrangement of the perforations varies: as porosity increases, the perforations approach the midpoint. Experiments and computational results indicate that rigidity remains constant or increases with increasing porosity. Notably, Pattern 5 has reduced material usage compared to Pattern 1 yet

demonstrates significantly enhanced rigidity. Figure 9 illustrates the difference between these two patterns. A higher load of $F = 0.5\,\text{N}$ was applied to the structures, leading to the failure of Pattern 1, whereas Pattern 5 experienced only modest deformation, measured in a few millimeters.

5. Conclusion

This paper examined the rigidity of various perforated kirigami sheets as bending-active, elastica-shaped arches under concentrated loads. Motivated by recent advancements aimed at achieving architectural configurations using elastica shapes realized by solid and perforated kirigami sheets, this work underscores the need for a profound understanding of load-bearing behavior and careful design considerations regarding the size and positioning of perforations. We employed a nonlinear beam model to examine the structural rigidity and proposed a method to approximate the effective load-bearing area of the sheet. Introducing holes onto the sheet induces multiple impacts on structural rigidity: material removal reduces local stiffness and self-weight while also influencing the structure's overall shape. We aimed to investigate the contradictory nature of this behavior: while the inclusion of holes typically reduces rigidity, it can also yield a more favorable shape, leading to increased rigidity. To address this issue, we designed multiple patterns to examine the effect of material removal and the location of the holes separately. Our findings reveal that these two factors exhibit comparable influences on the structure's rigidity. Consequently, a direct comparison of structural rigidity between two configurations cannot solely rely on assessing the removed material amount. Finally, we supported our findings by presenting a series of patterns where the pattern with higher porosity accounted for higher rigidity.

Kirigami structures hold significant promise for engineering applications, offering a versatile approach to designing lightweight, mobile structures that are easy to assemble. These structures apply to various fields, including aerospace, architecture and robotics. In architecture, kirigami structures facilitate the creation of innovative building façades, shading systems, and deployable or kinetic structures. Understanding the load-bearing behavior of kirigami structures is inevitable for exploiting their full potential.

Acknowledgments

References

[1] T.-U. Lee, J. M. Gattas, and Y. M. Xie, "Bending-active kirigami," *International Journal of Solids and Structures*, vol. 254-255, p. 111 864, 2022, ISSN: 00207683. DOI: 10.1016/j.ijsolstr.2022.111864.

[2] M. Bi, Y. He, Z. Li, T.-U. Lee, and Y. M. Xie, "Design and construction of kinetic structures based on elastica strips," *Automation in Construction*, vol. 146, p. 104 659, 2023.

[3] F. Ye, J. Chang, and Z. Fan, "Kirigami-based inverse design for 3d surfaces formed by mechanically guided method," *Thin-Walled Structures*, vol. 196, 2024, ISSN: 02638231. DOI: 10.1016/j.tws.2023.111462.

[4] Y. Zhang, J. Yang, M. Liu, and D. Vella, "Shape-morphing structures based on perforated kirigami," *Extreme Mechanics Letters*, vol. 56, Oct. 2022, ISSN: 23524316. DOI: 10.1016/j.eml.2022.101857.

[5] M. Liu, L. Domino, and D. Vella, "Tapered elasticæ as a route for axisymmetric morphing structures," *Soft Matter*, vol. 16, no. 33, pp. 7739–7750, 2020.

[6] F. Marmo, V. Perricone, A. Cutolo, M. D. C. Carnevali, C. Langella, and L. Rosati, "Flexible sutures reduce bending moments in shells: From the echinoid test to tessellated shell structures," *Royal Society Open Science*, vol. 9, 5 2022, ISSN: 20545703. DOI: 10.1098/rsos.211972.

[7] P. Celli *et al.*, "Shape-morphing architected sheets with non-periodic cut patterns," *Soft Matter*, vol. 14, pp. 9744–9749, 48 2018, ISSN: 17446848. DOI: 10.1039/c8sm02082e.

[8] C. Mcmahan, A. Akerson, P. Celli, B. Audoly, C. Daraio, and C. McMahan, "Effective continuum models for the buckling of non-periodic architected sheets that display quasi-mechanism behaviors," *Journal of the Mechanics and Physics of Solids*, vol. 166, 2022. DOI: 10.1016/j.jmps.2022.104934. [Online]. Available: https://hal.science/hal-03822700.

[9] J. Tao, H. Khosravi, V. Deshpande, and S. Li, *Engineering by cuts: How kirigami principle enables unique mechanical properties and functionalities*, Jan. 2023. DOI: 10.1002/advs.202204733.

[10] H. Cho and D. N. Kim, "Controlling the stiffness of bistable kirigami surfaces via spatially varying hinges," *Materials and Design*, vol. 231, Jul. 2023, ISSN: 18734197. DOI: 10.1016/j.matdes.2023.112053.

[11] Y. Hong, Y. Chi, S. Wu, Y. Li, Y. Zhu, and J. Yin, "Boundary curvature guided programmable shape-morphing kirigami sheets," *Nature Communications*, vol. 13, 1 Dec. 2022, ISSN: 20411723. DOI: 10.1038/s41467-022-28187-x.

[12] T. Yoneda, Y. Miyamoto, and H. Wada, "Structure, design, and mechanics of a pop-up origami with cuts," *Physical Review Applied*, vol. 17, 2 Feb. 2022, ISSN: 23317019. DOI: 10.1103/PhysRevApplied.17.L021004.

[13] B. Shrimali, M. Pezzulla, S. Poincloux, P. M. Reis, and O. Lopez-Pamies, "The remarkable bending properties of perforated plates," *Journal of the Mechanics and Physics of Solids*, vol. 154, p. 104514, 2021, ISSN: 0022-5096. DOI: https://doi.org/10.1016/j.jmps.2021.104514. [Online]. Available: https://www.sciencedirect.com/science/article/pii/S0022509621001782.

[14] P. Howell, G. Kozyreff, and J. Ockendon, *Applied solid mechanics*. Cambridge University Press, 2009.

[15] H. Uecker, D. Wetzel, and J. D. M. Rademacher, "Pde2path - a matlab package for continuation and bifurcation in 2d elliptic systems," *Numerical Mathematics: Theory, Methods and Applications*, vol. 7, no. 1, pp. 58–106, 2014. DOI: 10.1017/S1004897900000295.

[16] T. A. Driscoll, N. Hale, and L. N. Trefethen, "Chebfun guide," 2014.

[17] A. Vegt, van der and L. Govaert, *Polymeren : van keten tot kunststof*, Nederlands, 5e dr. / A.K. van der Vegt en L.E. Govaert. DUP Blue Print, 2003, ISBN: 90-407-2388-5.

[18] D. Vella, A. Boudaoud, and M. Adda-Bedia, "Statics and inertial dynamics of a ruck in a rug," *Physical review letters*, vol. 103, no. 17, p. 174301, 2009.